Performance of MgO and MgO-SiO_2 systems containing seeds under different curing conditions

G.V.P. Bhagath Singh[a], C. Sonat[a], E.H. Yang[a], C. Unluer[a,*]

[a] School of Civil and Environmental Engineering, Nanyang Technological University, 50 Nanyang Avenue, Singapore 639798, Singapore

* Corresponding author. Tel.: +65 91964970, E-mail address: ucise@ntu.edu.sg

Abstract

This study investigated the strength and microstructural development of MgO and MgO-microsilica (MS) systems under sealed and carbonated conditions. The influence of hydromagnesite seeds on the performance of each system was also evaluated. The hydration mechanisms were studied via isothermal calorimetry. A correlation between the strength development and formation of different phases was established. XRD, TG/DTG, FTIR and SEM were used for the identification and quantification of different hydrate and carbonate phases. MgO systems relied on the conversion of brucite into carbonate phases for their strength development, whereas M-S-H was the main source of strength in MgO-MS systems. The effect of seeding was evident in MgO-MS systems, where the extra space provided by the seeds increased the rate and degree of hydration. The formation of M-S-H was responsible for strength development and denser microstructures, which could be further improved via the increased utilization of unreacted MgO and MS.

Keywords: MgO; Hydration; Carbonation; Compressive strength; Microstructure

1. Introduction

Reactive magnesium oxide (MgO)-based binders have obtained significant attention due to their potential to be an alternative to ordinary Portland cement (OPC) in certain applications [1]. The major benefits of MgO cement in comparison to OPC are the relatively lower calcination temperatures used during its production (i.e. 700-900 vs. 1450 °C) and its ability to gain strength by sequestering carbon dioxide (CO_2) in the form of stable products [2, 3].

Hydration of MgO, which results in the formation of brucite, provides very limited strength in formulations, where MgO is used as the main binder [4]. One methodology that significantly improves the mechanical performance of MgO-based binders is the introduction of carbonation curing, which gives rise to the formation of hydrated magnesium carbonates (HMCs) subsequent to MgO hydration, as shown in Equations 1-5 [5]. The significance of HMCs in providing strength relies on the reduction in porosity associated with the volume expansion during their formation and the interlocking network they provide throughout the microstructure [3, 6]. A significant portion of the strength gain observed in MgO-based samples is generally completed within a few days of CO_2 curing [7]. Due to the need to use accelerated carbonation curing involving elevated levels of CO_2 for rapid strength gain, these samples can be more suitable for precast applications.

$$MgO + H_2O \rightarrow Mg(OH)_2 \text{ (Brucite)} \quad (1)$$

$$Mg(OH)_2 + CO_2 + 2H_2O \rightarrow MgCO_3 \cdot 3H_2O \text{ (Nesquehonite)} \quad (2)$$

$$2Mg(OH)_2 + CO_2 + 2H_2O \rightarrow Mg_2CO_3(OH)_2 \cdot 3H_2O \text{ (Artinite)} \quad (3)$$

$$5Mg(OH)_2 + 4CO_2 \rightarrow Mg_5(CO_3)_4(OH)_2 \cdot 4H_2O \text{ (Hydromagnesite)} \quad (4)$$

$$5Mg(OH)_2 + 4CO_2 + H_2O \rightarrow Mg_5(CO_3)_4(OH)_2 \cdot 5H_2O \text{ (Dypingite)} \quad (5)$$

Another alternative use of MgO as a binder is along with SiO_2 in the initial mix composition. In the presence of water, the MgO-SiO_2 system results in the formation magnesium silicate hydrate (M-S-H), which provides a significant strength gain. M-S-H formation takes place via the reaction between a magnesium source (e.g. Mg^{2+}, $Mg(OH)_2$) and the dissolved silica ions (SO_4^-), in which the commonly used superplasticizer, sodium hexametaphosphate (SHMP), plays a crucial role by leading to the formation of hydration products at lower water contents [8]. MgO-SiO_2 based binders can be effectively utilized in refractory castables [9] and other applications, where relatively lower pH values (i.e. ~10.5-11.0) are required, such as waste encapsulation [10, 11] and cementitious materials incorporating biodegradable fibers [12, 13]. Furthermore, MgO-SiO_2 based binders have the potential to be used as a cementitious binder in building applications due to their satisfactory fresh and hardened properties [14, 15].

Hydration of MgO is a dissolution-precipitation based process, leading to the formation of brucite, which can further react with the dissolved silica or carbonates, depending on their availability [16, 17]. Under ambient conditions, MgO hydration is limited to ~80% due to the precipitation of $Mg(OH)_2$ on the unhydrated MgO particles, which prohibits further contact with water [18-20]. With the incorporation of carbonation curing, precipitation of HMCs over brucite particles also inhibits the continuation of hydration and carbonation [6, 7]. Hence, both the carbonation and hydration reactions could cease before the raw materials are fully utilized, which results in an inefficient use of the binder.

In order to enhance the formation of both hydration and carbonation products, nucleation seeds can be introduced into the mix design. Seeds provide extra nucleation sites within the pore solution, which increases the available surface area for the precipitation of hydration and carbonation products. Previous studies have shown that the inclusion of calcium silicate hydrate (C-S-H) seeds can

improve early hydration within PC and alkali-activated slag systems [21, 22]. Recent studies [7, 23] that incorporated up to 1% of hydromagnesite seeds within carbonated MgO samples demonstrated enhanced carbonate formation, leading to 33% higher 28-day compressive strengths in comparison to unseeded samples. Although these initial studies reported the potential benefits of seeding on the performance of carbonated MgO systems, a comprehensive study focusing on the significance of seeding on both MgO and MgO-SiO_2 systems under carbonated and ambient curing conditions has not been reported yet.

The fast strength development of carbonated MgO samples necessitates the use of elevated CO_2 conditions, while the formation of M-S-H solely relies on the hydration reaction and does not require any special curing arrangements. As the formation of both HMC phases and M-S-H involve the same precursor (i.e. MgO) and initiate with the hydration of MgO, the two systems (i.e. carbonated MgO and MgO-SiO_2) indicate similarities in reaction patterns. In this respect, their combination in a single formulation can be beneficial in terms of mechanical performance and microstructural development. The synergy of these systems was previously investigated, in which the coexistence of the final products of both systems (HMCs and M-S-H) was reported [17]. Accordingly, the incorporation of CO_2 curing in the MgO-SiO_2 system resulted in improved strength development, which was more significant at early ages (i.e. 3 days), leading to ~60% increase in compressive strength. However, this study did not include the incorporation of nucleation seeding to improve the reaction mechanisms and the associated formation of hydration/carbonation products and did not provide a comparison with OPC-based mixes.

Therefore, the combination of these two systems (i.e. carbonated MgO and MgO-SiO_2) and their effect on the performance and microstructural development of concrete samples in the presence of nucleation seeding is worth further investigation. As a part of this approach, the link between the formation of different phases and strength gain in MgO and MgO-SiO_2 systems needs to be established.

In line with this goal, this study aims to investigate the properties of MgO and MgO-SiO_2 based binder systems with and without the inclusion of seeds. The influence of seeding was evaluated via a detailed analysis of MgO and MgO-SiO_2 based binder systems under carbonated and ambient curing conditions, which were also compared to OPC-based samples to provide a benchmark.

As a part of the experimental work, the mechanical performance of the concrete samples was examined via compressive strength testing at different durations up to 28 days. The progress of hydration reaction was initially evaluated via isothermal calorimetry. The link between the formation of different phases and strength development was established via a detailed microstructural analysis involving various qualitative and quantitative techniques. The quantification of the contents of hydrate and carbonate phases was performed via X-ray diffraction (XRD) and thermogravimetric/derivative thermogravimetric analysis (TG/DTG). The morphology of the selected samples was observed by field emission scanning electron microscopy (FESEM). Fourier-transform infrared spectroscopy (FTIR) was used to identify the chemical bonds within each sample to improve the understanding of the effect of carbonation curing and seeding on MgO and MgO-SiO_2 systems.

2. Materials and Methodology

Reactive MgO supplied by Richard Baker Harrison (UK) and micro silica (MS) obtained from Elkem (Singapore) were used as the main raw materials to produce the binder. The chemical and physical properties of these materials are listed in Table 1. Reagent grade (> 98%) hydromagnesite (HM) seeds supplied by Fisher Scientific (UK) with a surface area of 43.5 m^2/g were used to provide additional nucleation sites within the prepared mixes. Coarse aggregates with a particle size of 4.7–9.5 mm were used in the preparation of concrete samples. Fine aggregates

were omitted from the mix design to avoid any quartz contamination during the quantification of phases.

The particle size distributions of MgO, MS and hydromagnesite seeds are shown in Fig. 1. It can be seen that MgO and hydromagnesite seeds had relatively comparable particle size distributions, whereas MS revealed higher particle sizes when compared to the others. The calculated different size fractions of these materials are listed in Table 2.

Two sets of binders were prepared consisting of (i) MgO and (ii) MgO-MS at a ratio of 1:1 (i.e. by mass). Hydromagnesite seed was added at a content of 1% (i.e. by mass) of the total binder content to assess the effect of seeding in comparison to mixes that did not include any seed addition. The detailed binder compositions used in the preparation of samples are listed in Table 3. Along with these, an OPC-based mix was prepared for comparison purposes. A water to binder (w/b) ratio of 0.46 was used in all mixes. Sodium hexametaphosphate (SHMP), was included at an amount of 1.2% (i.e. by mass) of the total binder content to improve the fluidity of Mg-based mixes, in line with the findings of previous research [17, 24].

Concrete samples consisting of 40% binder and 60% aggregates by mass were prepared by mixing the dry ingredients in a pan mixer first, followed by the gradual addition of water. Prior to the mixing process, the aggregates were washed several times and dried at room temperature to remove all impurities. Mixing was carried out until a homogenous mix was obtained. The prepared mix was placed into 50x50x50 mm cubic moulds, which were placed under two different curing conditions under a constant temperature of 30±1 ºC and relative humidity of 95±1%: (i) sealed curing at atmospheric CO_2 concentration and (ii) accelerated curing at 10% CO_2 concentration.

Compressive strength development was evaluated at 3, 7 and 28 days. To obtain each data point, five samples were tested and their average was reported, for

which the deviation was lower than 1.5 MPa. Fragments obtained from the 3-day (i.e. representing “early” strength) and 28-day (i.e. representing “late” strength) cubic specimens after strength testing were used for microstructural analysis. Coarse aggregates were separated from the binder portion to avoid any quartz contamination in the quantification of phases. Since carbonation is a diffusive process, 50% of the fragments were collected from the core of the samples, whereas the rest were obtained from the sample surfaces, thereby providing a representative selection of the entire carbonation profile. The collected fragments were submerged in isopropanol to stop hydration, followed by drying in a vacuum chamber. Selected fragments were used in FESEM analysis, whereas the rest was ground to pass a sieve size of 75 μm to be used in XRD, TG/DTG and FTIR analyses.

Magnesium silicate hydrate (M-S-H) gel was synthesized for comparison purposes [8]. Sodium metasilicate pentahydrate and magnesium chloride were mixed in deionized water at a Mg:Si molar ratio of 3:2. The solution was stirred for 45 minutes before being put aside for the gel to settle. Excess water was then removed and the extracted gel was placed in a test tube to undergo washing with deionized water for the removal of dissolved ions. The centrifuging and washing processes were repeated 6 times, after which the obtained M-S-H gel was filtered and vacuum dried.

Heat flow associated with the hydration reaction was measured by using an I-Cal 8000 High Precision Calorimeter at a temperature of 26 ºC. The paste samples corresponding to each mix design, as listed in Table 3, were prepared and placed into individual chambers within 30 seconds to measure the heat of hydration.

XRD measurements were performed on powder samples using a Bruker D8 Advance instrument, consisting of a LynxEye super positioned detector with Cu-Kα-radiation. The scanned range was set between 10º and 70º 2θ, at a step size of 0.02º 2θ and increments of 90 seconds/step. The X-ray tube generator was

operated at 40 kV and 40 mA. The crystalline phases were identified using the Powder Diffraction File-2. The external standard method was used for the quantification of both crystalline and amorphous phases [26-28]. During this process, corundum was used as the external standard. Rietveld quantitative phase analysis was performed using TOPAS 5 software. Crystal structures of known phases were taken from the Inorganic Crystal Structure Database (ICSD). Pseudo Voigt was used to fit the crystalline and amorphous phases. Chebyshev polynomial combined with a 1/2θ term was used to fit the background intensity. The goodness of the fit was judged by viewing the observed and calculated patterns and using the difference curve [29]. The bound water content, determined by the mass loss at 50-600 ºC, was included in the calculation of hydrated phases and the mass absorption coefficient of hydrated samples.

A Perkin Elmer TGA 4000 instrument with a heating rate of 10 º/min from 30 to 900 ºC was used under nitrogen flow to determine the thermal decomposition patterns in the prepared samples. The IR spectrum was measured via a Perkin Elmer spectrometer using ATR mode. The scans were obtained by taking the average of 16 scans within a wavelength range of 650 to 4000 cm^{-1}, with a step size of 1.9 cm^{-1}. The morphologies of the formed hydrate and carbonate phases were observed via FESEM using a JEOL JSM-7600F microscope. The fragments obtained from each sample were attached to a carbon tape, followed by coating their surfaces with gold before analysis.

3. Results and Discussion

3.1 Characterization of raw materials

The typical XRD spectra of MgO, MS and hydromagnesite seeds are shown in Fig. 2, whereas the phase quantification values obtained by Rietveld refinement are listed in Table 4. Different crystalline phases were observed in the MgO sample in

Fig. 2(a), which were mainly identified as periclase (PDF-01-077-2364) and magnesite (PDF-01-086-0175). MS revealed a broad amorphous hump over a 2θ range of 15-35º, as shown in Fig. 2(b). This broad hump represented the glassy portion of the sample. Pawley intensity profile was used to fit the total amorphous portion of MS. The peak position of SiO_2-rich glass was at ~22º 2θ [30], whereas there were not any SiO_2-based crystalline phases present in the system. The main SiO_2 phase was in the form of reactive SiO_2, whose content and total glassy portion are listed in Table 4. The hydromagnesite seed consisted of mainly hydromagnesite (PDF-01-070-0361) with almost no impurities present in the system, as shown in Fig. 2(c). In addition to the raw materials used in the preparation of samples, the XRD pattern of the synthesized M-S-H is shown in Fig. 2(d). The presence of M-S-H was observed via the amorphous portion over a 2θ angle range between 20-30º, 33-40º and 58-62º, which was in line with the findings of previous studies [13, 15, 31, 32]. Pawley intensity refinement performed on MS and M-S-H revealed the peak positions listed in Table 5, which showed that some of the unreacted silica was not fully converted to M-S-H during its synthesis. This led to the appearance of two humps within the 15-30º 2θ region. The first peak was associated with the presence of the unreacted SiO_2, whereas the second hump was due to the formation of M-S-H. Similar observations were reported by previous studies [9, 13, 31], where the locations of the three main humps allocated to M-S-H were defined in the 2θ range of 15-30º, 33-40º and 58-62º [9, 13, 31].

The typical SEM images of MgO, MS and hydromagnesite seed are shown in Fig. 3. MgO revealed a uniform distribution of particles with uneven shapes and different sizes (Fig. 3(a)). Alternatively, MS was composed of spheres of different sizes with well-defined boundaries (Fig. 3(b)). The morphology of hydromagnesite seeds differed from the others as it contained dense agglomerations of disk-like structures (Fig. 3(c)).

3.2 Analysis of samples

3.2.1 Isothermal calorimetry

The heat flow curves of all paste samples are shown in Fig. 4(a). The dissolution of particles occurred in the first few hours, followed by the precipitation of hydrate phases. The acceleration period showed variations depending on the binder component. The OPC mix hydrated earlier than all MgO-based mixes, which was associated with the slower reaction of MgO as a binder. When compared to the sole use of MgO, MgO-MS mixes led to higher peaks in the acceleration period. The addition of hydromagnesite seed had a positive effect on the reaction mechanism, which was revealed by the earlier appearance of the hydration peak in both systems. The effect of seeding was more obvious in the MgO-MS system, where a higher and earlier (i.e. 38 hours) hydration peak was observed when compared to the unseeded mix (i.e. 50 hours). These findings were in line with the results reported by earlier studies [21, 23], where the role of seeds in accelerating the hydration reaction in different systems was reported.

The cumulative heat curves of MgO, MgO-MS and OPC mixes over a period of 72 hours are shown in Fig. 4(b). All mixes showed a gradual increase in their heat of hydration over time, whereas the slope corresponding to the main peak was earlier and higher for the OPC mix. Although the OPC mix had revealed a shorter induction period accompanied with a higher main hydration peak during the first 24 hours, its cumulative heat after 48 hours was lower than MgO-MS mixes. As observed earlier in the heat flow patterns, the heat released by MgO-MS mixes was significantly higher than MgO mixes, which could be due to the formation of M-S-H in addition to brucite in the former system. While the addition of seeds had a clear effect on the extent of hydration in both systems, it was more influential in the MgO-MS system. Accordingly, the use of seeds in these systems not only led to an earlier increase in the cumulative heat, but also increased the rate of heat release, thereby resulting in a higher heat of hydration from 24 hours onwards.

3.2.2 Compressive strength

The effect of seeding on the strength development of MgO and MgO-MS systems in comparison with the OPC mix under sealed conditions is shown in Fig. 5(a). A steady increase in strength was observed in all mixes with age, during which the OPC mix reached a 28-day strength of 36 MPa. MgO-based mixes, with and without the inclusion of seeds, revealed lower strengths than the other mixes, which was associated with the limited formation of brucite under sealed conditions. While the early (i.e. 3-day) strength of the MgO-MS mix was similar to that of the OPC mix at 16 MPa, this system achieved a higher strength than the OPC mix from 7 days onwards. Accordingly, MgO-MS mixes reached 28-day strengths of 55 and 44 MPa with and without the inclusion of seeds, respectively. The positive effect of seeds in the strength development of MgO-MS mixes was obvious from 3 days onwards, which led to ~25% increase in the overall 28-day strength in comparison to unseeded MgO-MS samples. Alternatively, seeding did not have any obvious influence on the strength of MgO-based mixes cured under the same conditions, whose strength development was hindered by the limited dissolution of MgO and the associated formation of brucite.

A different scenario was observed when carbonation curing was introduced in the prepared mixes with and without the inclusion of seeds. A comparison of all Mg-based samples with OPC mixes is shown in Fig. 5(b). A steady increase in strength was observed in all mixes with age, although carbonation slowed down after the first 7 days of curing, which was in line with the observations of earlier studies [7]. The use of carbonation curing had the highest influence on MgO and MgO-HM mixes, which experienced a 197-163% increase in their 28-day strengths via the use of 10% CO_2 during the curing process. Alternatively, carbonation was less influential in the strength development of MgO-MS and OPC mixes, whose performance was mainly dependent on the formation of hydrate phases such as

M-S-H and C-S-H, respectively. Within these samples, a very little difference in early and 28-day strength was observed under both curing conditions. On the other hand, carbonated MgO samples (MgO-C) achieved a very rapid increase in strength at early ages (i.e. 3 days), which was further enhanced with the inclusion of seeds in samples MgO-HM-C. Accordingly, this translated into 288% increase in the 3-day strength of MgO-C when compared to uncarbonated MgO samples (31 vs. 8 MPa); and 320% increase in the corresponding strength of MgO-HM-C when compared to uncarbonated MgO-HM samples (42 vs. 10 MPa). A similar trend was observed in the longer period at 28 days of curing, during which these samples revealed strengths of up to 56-60 MPa, in comparison to 19-22 MPa observed in the corresponding samples cured under uncarbonated/sealed conditions.

Overall, these results highlighted the important role of carbonation curing in the strength development of MgO-based mixes; whereas the influence of seeds had a larger role in MgO-MS mixes. The reason for the increase in strength in the former case could be associated with the formation of hydrated magnesium carbonate (HMC) phases, which were identified as the main source of strength in carbonated MgO systems [3, 4, 6]. Alternatively, MgO-MS mixes achieved strength via the formation of M-S-H, whose formation could be enhanced with the provision of additional nucleation sites under the presence of seeds provided within the MgO-MS-HM sample. When compared to OPC samples cured under sealed and carbonated conditions, samples MgO-MS-HM (i.e. cured under sealed or carbonated conditions), MgO-C and MgO-HM-C achieved higher strengths. This could be an indication for the potential use of Mg-based binders in certain applications, where similar or higher strengths than OPC-based formulations can be provided.

3.2.3 X-ray diffraction

The XRD spectra of MgO powder as well as MgO-based samples with and without the addition of seeds cured under sealed and carbonated conditions for 3 and 28 days are shown in Fig. 6(a). The MgO power primarily consisted of periclase and magnesite as its major phases, along with illite (PDF-00-002-0050) as a minor phase. Samples cured under sealed conditions revealed the presence of brucite (PDF-01-076-0667), periclase (PDF-01-077-2364) and magnesite (PDF-01-086-0175). Samples subjected to carbonation contained HMC phases such as hydromagnesite (PDF-01-070-0361), along with nesquehonite (PDF-00-001-0130), artinite (PDF-01-072-1320) and dypingite (PDF-00-029-0857). These observations were in agreement with the phases reported in previous studies [4, 5, 7, 26], where brucite was reported as the main hydrate phase under sealed conditions, along with the formation of HMCs under carbonation conditions.

The representative refined spectra of a selected MgO-HM sample subjected to carbonation curing for 3 days are shown in Fig. 6(b) to serve as an example of how phase quantification was performed on each sample. The obtained phase quantities within each sample are listed in Table 6. A reduction in the periclase content over time was an indication of the continuation of hydration/carbonation within the prepared samples. This was accompanied with an increase in the brucite content with curing duration, under both curing conditions. The use of carbonation curing led to a lower periclase content in MgO samples, which could be partially ascribed to the formation of carbonate phases over time. The relatively fixed magnesite content in all samples was an indication of its presence as undecomposed parent material within the original MgO powder, as indicated earlier in Table 4. The addition of seed did not have a major influence on the utilization of MgO, as the periclase contents in seeded and unseeded samples were comparable; whereas it led to a very slight increase in the formation of brucite and carbonate phases. The negligible effect of seeds in the measured contents of reaction products could be partially due to issues associated with sample preparation. Accordingly, a blend of powders taken from the inner core (i.e. least carbonated) and the outside exterior (i.e. most carbonated) sections were used for

the preparation of samples that were representative of the entire sample cross-section for XRD analysis. This approach could have led to an underestimation of the carbonate phases, which could be more pronounced depending on the proportion of powders taken from the inner core.

The XRD spectra of MgO-MS samples cured under sealed and carbonated conditions for 3 and 28 days, as well as those of MS and synthesized M-S-H are shown in Fig. 7(a). In all samples, broad amorphous humps were observed in the 2θ range between 15-30º, 33-40º and 58-62º, which were associated with the presence of M-S-H [9, 13]; along with various crystalline phases. Crystalline phases mainly consisted of periclase, magnesite, dypingite, nesquehonite and brucite. The formation of M-S-H took place via the hydration of MgO in the presence of SiO_2 supplied by MS. Accordingly, the amorphous hump observed in the XRD spectra of the analyzed samples was a combination of the glassy portion of MS and M-S-H. These observations were in line with the findings reported in previous studies [15, 17]. A portion of the 2θ angle ranging from 15º to 30º was attributed to the unreacted glassy phases within MS, which overlapped with the formation of M-S-H [9, 13, 15, 32-36].

The representative refined spectra of a selected MgO-MS-HM sample subjected to sealed conditions for 3 days are shown in Fig. 7(b). Phase quantification was performed on all mixes, during which the amorphous phases (i.e. fitted using Pawley intensity profile) were calculated along with the crystalline ones. A peak fit algorithm, which used unconstrained non-linear optimization, was employed to decompose the broad x-ray diffraction pattern in the 15-30º 2θ range. The regression coefficient (r^2) varied between 0.999 and 0.998 using PV fit. The intensity contribution of each component to the total intensity pattern of the amorphous phase was obtained by the decomposition of the total intensity signature as a sum of fundamental underlying PV peak shapes. Two PV peaks were fitted to the intensity profile in this region using the peak fit algorithm. The use of additional peaks did not result in any improvements to the overall fit. A

similar approach in the quantification of amorphous phases was reported in earlier studies [37, 38]. The deconvolution of the amorphous portion in the 15-30º 2θ range is shown in Fig. 7(c). Results obtained from the decomposition of the total amorphous phase into component PV peaks clearly indicated the presence of two distinct peaks. The peak at the lower 2θ angle was associated with the glassy portion of MS and the second peak at the higher 2θ angle was produced by M-S-H. Accordingly, one peak was obtained between 21 and 22º 2θ and the second peak was centered between 25 and 26º 2θ. These peak positions were in perfect alignment with the actual profiles listed earlier in the Table 5. The glassy content in the system was determined using the area under the unreacted glass with respect to the total area of the spectrum. The total M-S-H content was determined via a calculation of the total area under the M-S-H profile with respect to the total area of the spectrum. The total M-S-H area was calculated as the sum of areas under each M-S-H hump (as seen in Fig. 7(b)) and M-S-H profile (as seen in Fig. 7(c)).

The obtained phase quantities within each MgO-MS sample are listed in Table 7. When compared to MgO samples (Table 6), lower periclase contents were observed in MgO-MS samples, which was associated with the increased hydration/carbonation reactions, as well as the lower initial MgO content of the latter. A steady decline in the periclase content with age in all the mixes was a representation of the progress of hydration (i.e. under sealed conditions) and carbonation (i.e. under carbonated conditions). This was accompanied with an increase in the brucite content from 3 to 28 days in all the mixes, albeit at much lower amounts than those observed earlier in MgO samples. Minor formations of HMC phases such as hydromagnesite, dypingite and nesquehonite was observed in carbonated samples, which may have contributed to the strength development of MgO-MS samples over time. The decline in the unreacted glassy content was accompanied with an increase in the amount of M-S-H with age under both curing conditions, which was an indication of the progress of hydration. Unlike the MgO samples, the addition of seeds had an influence in the formation of M-S-H within

MgO-MS samples. This was particularly observed at 28 days, during which a clear reduction in the amount of unreacted glass content and an increase in M-S-H content was revealed with the introduction of seeds. This contribution of seeds to the reaction mechanisms within MgO-MS samples was also observed earlier in the isothermal calorimetry and strength results, where it was shown that the presence of seeds improved the reaction mechanism, which led to increased strength gain. These findings were a clear indication of the role of M-S-H in providing strength, as well as the positive influence of seeds in increasing the surface area for the enhanced formation of M-S-H in MgO-MS systems. Nevertheless, a considerable amount of unreacted glass and periclase was present in these samples even after 28 days, indicating that the continued progress of hydration enabled via the availability of these phases could result in an even better performance in the longer term.

3.2.4 Thermogravimetric analysis

The representative TG/DTG curves of MgO and MgO-MS samples cured under carbonated conditions for 28 days are shown in Fig. 8. Four major predominant endothermic peaks were observed on the DTG curves over the temperature ranges of 50-340, 340-480, 480-600 and 600-700 ºC. Each of these endothermic peaks represented the decomposition of the hydrate and carbonate phases within these systems. The mass loss corresponding to the 50-340 ºC range was associated with the dehydration of M-S-H in MgO-MS samples [39-42]. The loss between 340-480 ºC was attributed to the dehydration of brucite and HMCs [41-44]. This was followed by the changes in the 480-600 ºC region, which were due to the dehydroxylation of HMCs such as hydromagnesite and dypingite [42, 44]. Finally, the mass loss in the temperature range of 600-700 ºC was mainly because of the decarbonation of magnesite and HMCs that formed during carbonation curing [45, 46].

The mass loss values corresponding to each of these different temperature ranges in all samples subjected to sealed and carbonated curing for 3 and 28 days are listed in Table 8. An increase in the mass loss was observed over time in all samples, which was associated with the continuation of the hydration and carbonation reactions from 3 to 28 days. In the temperature range of 50-340 ºC, a higher mass loss was revealed by the MgO-MS samples when compared with the MgO samples. This increased mass loss was attributed to the formation of M-S-H in the MgO-MS system. Carbonated samples generally showed slightly higher mass loss values than those cured under sealed conditions, which was due to the formation of HMCs. In line with the trends observed in their strength development, MgO samples did not reveal a significant increase in mass loss over time except for the 340-480 ºC range, which was an indication of the increased formation of brucite, explaining the limited strength development of these samples. Alternatively, MgO-MS samples indicated a steady increase in mass loss over time, especially within the 50-340 ºC range, which was associated with the decomposition of M-S-H. The introduction of carbonation curing led to an increase in the lass loss values observed within the 600-700 ºC range, referring to the decarbonation of strength providing carbonate phases.

A comparison of the brucite contents obtained from TGA and XRD-based Rietveld analysis is displayed in Table 9. In the case of TGA, the mass loss occurring within the 340-480 ºC range was associated with the dehydration of brucite (i.e. considering the minor loss associated with the dehydration of the limited formation of HMCs). While variations in the values obtained by each approach was observed due to the different calculation methods, the trends revealed were the same in each method. The values corresponding to the brucite content within MgO samples were comparable with little difference across the two methods. Alternatively, those within MgO-MS samples showed variations, in which the values obtained by TGA were higher than those obtained via Rietveld analysis. The higher values revealed by TGA could be attributed to the decomposition of HMCs as well as the partial contribution of M-S-H dehydration in this temperature range, reflecting the

suitability and drawbacks of each method in the quantification of hydrate phases within MgO systems.

3.2.5 FTIR analysis

The FTIR spectra of MgO powder and MgO samples cured under sealed and carbonated conditions for 28 days are shown in Fig. 9(a). A wide range of bands were observed in the MgO power, which were also apparent in the prepared samples, along with additional bands. The band at ~3700 cm^{-1} was associated with the anti-symmetrical stretching of O-H bonds, referring to the formation of brucite [47-49]. Similarly, the presence of brucite was also linked with the small band at ~3650 cm^{-1}, which was attributed to the free O-H vibration [47-50]. Furthermore, the band at ~1650 cm^{-1} was due to the bending vibration of O-H [51, 52]. A few small bands were observed in the region from 1380 to 1450 cm^{-1}, which could be ascribed to the formation of different carbonate phases. The peak profile and band width between this region could show variations, depending on the type of carbonates [47-50]. The band at ~1120 cm^{-1} was due to the symmetrical stretching of the CO_3^{2-} ion [47, 53, 54], whereas the band at ~1015 cm^{-1} occurred due to the symmetrical stretching of CO_3^{2-} in the form of magnesium carbonate [47]. The band near 880 cm^{-1} was associated with CO_3^{2-} bending vibrations. These bands referred to the presence of partially crystalline phases, which were present in small quantities in the studied systems.

The FTIR spectra of MS powder, synthesized M-S-H and MgO-MS samples cured under sealed and carbonated conditions for 28 days are shown in Fig. 9(b). Different band widths were observed in the synthesized M-S-H and MS. For instance, a wide band at 800-1200 cm^{-1} was observed in M-S-H, whereas the corresponding band was at 900-1300 cm^{-1} in the case of MS. Another band at ~800 cm^{-1} in MS was revealed due to the Si-O-Si internal vibrations. The small band near 3695 cm^{-1} was related to the anti-symmetrical stretching of O-H bonds,

555 which was an indication of the formation of brucite. The band at ~1625 cm^{-1} was
556 attributed to the H-O-H bending vibration in the form of H_2O [31]. The band (i.e.
557 shoulder) at 3690 cm^{-1} was assigned to Mg-OH stretching vibrations in M-S-H [55,
558 56]. Bands located at ~2975, 1420 and 815 cm^{-1} represented the presence of
559 carbonates, via the occurrence of CO_3^{2-} bending vibrations [31].
560
561 Further detailed investigations were conducted in the wavelength range of 800-
562 1300 cm^{-1} to identify the different bands in MS, synthesized M-S-H and MgO-MS
563 samples. A non-liner fit algorithm was used to locate the different bands in this
564 region. The deconvoluted portions of MS and synthesized M-S-H involved the
565 fitting of three bands, as seen in Fig. 10(a) and (b), respectively. Additional fitting
566 of phases did not result in any improvement to the overall fit. The locations of the
567 observed bands are listed in Table 10. The bands observed in MS were attributed
568 to Si-O-Si internal vibrations [31]. In the case of synthesized M-S-H, the bands
569 were due to Si-O-Si bending vibrations [31, 57]. The deconvolution of a
570 representative MgO-MS sample cured under sealed conditions for 28 days, shown
571 in Fig. 10(c), revealed the presence of five different bands within the broad band.
572 These bands, attributed to Si-O-Si internal and bending vibrations, were within the
573 wavelength ranges observed in MS and synthesized M-S-H, as listed in Table 10.
574 Therefore, it could be concluded that the broad portion observed in MgO-MS
575 samples is a combination of M-S-H and unreacted SiO_2 glass. While the position
576 of the band could slightly vary depending on the Si coordination level, Mg/Si atomic
577 ratio and curing conditions, similar bands were observed in all MgO-MS samples.
578
579
580 **3.2.6 SEM analysis**
581
582 SEM analysis was carried out on selected MgO and MgO-MS samples to assess
583 the differences in their microstructures. Evaluation of their performance and
584 microstructural development revealed the positive influence of seeding in the MgO-
585 MS system, whereas the use of seeds was not very effective in the MgO system.

Alternatively, the introduction of carbonation curing led to strength gain via the formation of HMCs within MgO samples, which was not as critical in MgO-MS samples as their strength development was mainly dependent on the formation of M-S-H.

In line with these findings, the SEM images of MgO samples cured under sealed and carbonated conditions for 28 days are shown in Fig. 11. A clear difference in sample microstructure was observed, depending on the curing condition utilized. Accordingly, samples cured under sealed conditions mainly consisted of unhydrated MgO particles along with some hydrated particles. These partially reacted particles formed a sponge-like structure that resembled brucite, around the unreacted particles. These observations were in agreement with the results obtained via XRD analysis, where the dominating presence of brucite in MgO systems cured under sealed conditions was reported. The introduction of carbonation curing to these samples led to a much denser microstructure composed of a mixture of different phases, as seen in Fig. 11(b). Along with unhydrated MgO particles and uncarbonated brucite, major HMC phases such as the needle-like nesquehonite and rosette-like hydromagnesite/dypingite formations were observed [7, 17], which were in line with the XRD results.

Another parameter assessed was the effect of seeding in the microstructure of MgO-MS systems. This was evaluated via a comparison of the SEM images of MgO-MS and MgO-MS-HM samples, as shown in Fig. 12. While a dense microstructure was observed in both scenarios, the presence of unreacted MgO and MS could still be identified even after 28 days of curing, as also highlighted earlier by the quantification of phases via XRD analysis. Along with these particles, the wide presence of brucite was detected in unseeded samples, whereas the continuous network associated with the gel-like structure of M-S-H could easily be seen in seeded samples shown in Fig.12(b). The enhanced formation of M-S-H via the increased space provided by the presence of seeds led to a denser structure by filling in the available pores in MgO-MS samples. This improvement in

microstructure was in line with the higher strengths of these samples, which could explain the active role of seeds in enhancing the hydration and thereby the performance of MgO-MS systems.

4. Conclusions

The study investigated the performance and microstructural development of MgO and MgO-MS systems with and without the inclusion of nucleation seeds, under two different curing conditions. The use of carbonation curing led to the formation of carbonate phases, along with the major hydrate phases observed under sealed conditions. MgO systems mainly relied on the conversion of brucite into HMCs such as hydromagnesite and nesquehonite for strength development, while the formation of M-S-H was the main source of strength in MgO-MS systems. The effect of seeding was much more significant in MgO-MS samples, in which the presence of seeds increased the rate and degree of hydration by providing extra space for the enhanced formation of M-S-H. This not only led to an increase in the mechanical performance of the samples, but also enabled the formation of denser microstructures. The results indicated a direct link between strength development and M-S-H content in these samples, whereas the unreacted silica and periclase contents were revealed to be inversely proportional to performance. Overall, this study has highlighted the need to identify the right curing conditions within MgO systems, depending on the binder composition. In order to improve the use of MgO as a binder, further research should focus on the optimization of the parameters that will enable the complete utilization of MgO, thereby increasing the efficiency of the binder component and enhancing performance.

Acknowledgement

The authors would like to acknowledge the financial support from the Singapore MOE Academic Research Fund Tier 2 (MOE2017-T2-1-087 (S)) for the completion of this research project.

References

[1] S.A. Walling, J.L. Provis, Magnesia-based cements: a journey of 150 years, and cements for the future?, Chem. Rev., 116 (2016) 4170-4204.

[2] N. Dung, C. Unluer, Sequestration of CO_2 in reactive MgO cement-based mixes with enhanced hydration mechanisms, Constr. Build. Mater., 143 (2017) 71-82.

[3] C. Unluer, A. Al-Tabbaa, Enhancing the carbonation of MgO cement porous blocks through improved curing conditions, Cem. Concr. Res. 59 (2014) 55-65.

[4] M. Liska, L.J. Vandeperre, A. Al-Tabbaa, Influence of carbonation on the properties of reactive magnesia cement-based pressed masonry units, Adv. Cem. Res. 20 (2008) 53-64.

[5] M. Liska, A. Al-Tabbaa, Ultra-green construction: reactive magnesia masonry products, Waste and Resource Management 162 (2009) 185-196.

[6] C. Unluer, A. Al-Tabbaa, Impact of hydrated magnesium carbonate additives on the carbonation of reactive MgO cements, Cem. Concr. Res. 54 (2013) 87-97.

[7] N. Dung, C. Unluer, Development of MgO concrete with enhanced hydration and carbonation mechanisms, Cem. Concr. Res. 103 (2018) 160-169.

[8] Y. Jia, B. Wang, Z. Wu, J. Han, T. Zhang, L.J. Vandeperre, C.R. Cheeseman, Role of sodium hexametaphosphate in MgO/SiO2 cement pastes, Cem. Concr. Res. 89 (2016) 63-71.

[9] Y. Zhang, Y. Li, Y. Xu, S. Sang, S. Jin, Enhanced formation of magnesium silica hydrates (MSH) using sodium metasilicate and caustic magnesia in magnesia castables, Ceram. Int. 43 (2017) 9110-9116.

[10] T. Zhang, C.R. Cheeseman, L.J. Vandeperre, Development of low pH cement systems forming magnesium silicate hydrate (MSH), Cem. Concr Res. 41 (2011) 439.

[11] S.A. Walling, H. Kinoshita, S.A. Bernal, N.C. Collier, J.L. Provis, Structure and properties of binder gels formed in the system $Mg(OH)_2$–SiO_2–H_2O for immobilisation of Magnox sludge, Dalton Trans, 44 (2015) 8126-8137.

[12] T. Zhang, E. Dieckmann, S. Song, J. Xie, Z. Yu, C. Cheeseman, Properties of magnesium silicate hydrate (MSH) cement mortars containing chicken feather fibres, Constr. Build. Mater. 180 (2018) 692-697.

683 [13] G. Mármol, H. Savastano, M.M. Tashima, J.L. Provis, Optimization of the
684 MgO SiO_2 binding system for fiber-cement production with cellulosic reinforcing
685 elements, Mater. Des. 105 (2016) 251-261.
686 [14] H. Tran, A. Scott, Strength and workability of magnesium silicate hydrate
687 binder systems, Constr. Build. Mater. 131 (2017) 526-535.
688 [15] T. Zhang, L.J. Vandeperre, C.R. Cheeseman, Formation of magnesium
689 silicate hydrate (MSH) cement pastes using sodium hexametaphosphate, Cem.
690 Concr. Res. 65 (2014) 8-14.
691 [16] L. Amaral, I. Oliveira, R. Salomão, E. Frollini, V. Pandolfelli, Temperature and
692 common-ion effect on magnesium oxide (MgO) hydration, Ceram. Int. 36 (2010)
693 1047-1054.
694 [17] C. Sonat, C. Unluer, Investigation of the performance and thermal
695 decomposition of MgO and MgO-SiO_2 formulations, Thermochim. Acta 655
696 (2017) 251-261.
697 [18] F. Jin, A. Al-Tabbaa, Thermogravimetric study on the hydration of reactive
698 MgO and silica mixture at room temperature, Thermochim. Acta 566 (2013) 162.
699 [19] S.D.F. Rocha, M.B. Mansur, V.S.T. Ciminelli, Kinetics and mechanistic
700 analysis of caustic magnesia hydration, J. Chem. Technol. Biotechnol. 79 (2004)
701 816-821.
702 [20] F. Jin, A. Al-Tabbaa, Characterisation of different commercial reactive
703 magnesia, Adv. Cem. Res. 26 (2014) 101-113.
704 [21] M.H. Hubler, J.J. Thomas, H.M. Jennings, Influence of nucleation seeding on
705 the hydration kinetics and compressive strength of alkali activated slag paste,
706 Cem. Concr. Res. 41 (2011) 842-846.
707 [22] J.J. Thomas, H.M. Jennings, J.J. Chen, Influence of nucleation seeding on
708 the hydration mechanisms of tricalcium silicate and cement, The Journal of
709 Physical Chemistry C 113 (2009) 4327-4334.
710 [23] N. Dung, C. Unluer, Influence of nucleation seeding on the performance of
711 carbonated MgO formulations, Cem. Concr. Compos. 83 (2017) 1-9.
712 [24] N.T. Dung, C. Unluer, Improving the performance of reactive MgO cement-
713 based concrete mixes, Constr. Build. Mater. 126 (2016) 747-758.
714 [25] C. Sonat, N. Dung, C. Unluer, Performance and microstructural development
715 of MgO–SiO_2 binders under different curing conditions, Constr. Build. Mater. 154
716 (2017) 945-955.

[26] B.H. O'Connor, M.D. Raven, Application of the Rietveld Refinement Procedure in Assaying Powdered Mixtures, Powder Diffr. 3(1) (1988) 2-6.
[27] G.V.P. Bhagath Singh, K.V.L. Subramaniam, Characterization of Indian fly ashes using different experimental Techniques, Ind. Concr. J. 92(3) (2018) 10-23.
[28] G.V.P. Bhagath Singh, K.V.L. Subramaniam, Quantitative XRD Analysis of Binary Blends of Siliceous Fly ash and Hydrated Cement, J. Mater. Civil Eng. (ASCE) 28(8) (2016) 04016042 (1-7).
[29] B.H. Toby, R factors in Rietveld analysis: How good is good enough, Powder Diffr. 21(1) (2006) 67-70.
[30] P.T. Durdzinski, R. Snellings, C.F. Dunant, M. Ben Haha, K.L. Scrivener, Fly ash as an assemblage of model Ca-Mg-Na-aluminosilicate glasses, Cem. Concr. Res. 78 (2015) 263-272.
[31] D. Nied, K. Enemark-Rasmussen, E.L. Hopital, J. Skibsted, B. Lothenbach, Properties of magnesium silicate hydrates (M-S-H), Cem. Concr. Res. 79 (2016) 323-332.
[32] D.R.M. Brew, F.P. Glasser, Synthesis and characterisation of magnesium silicate hydrate gels, Cem. Concr. Res. 35 (2005) 85-98.
[33] W. Jiangxiong, C. Yimin, L. Yongxin, The reaction mechanism between MgO and microsilica at room temperature, J. Wuhan Univ. Technol. Mater. Sci. 21 (2006) 88-91.
[34] J. Temuujin, K. Okada, K.J.D. MacKenzie, Formation of layered magnesium silicate during the aging of magnesium hydroxide-silica mixtures, J. Am. Ceram. Soc. 81 (2005) 754-756.
[35] C. Roosz, S. Grangeon, P. Blanc, V. Montouillout, B. Lothenbach, P. Henocq, E. Giffaut, P. Vieillard, S. Gaboreau, Crystal structure of magnesium silicate hydrates (M-S-H): The relation with 2:1 Mg\Si phyllosilicates, Cem. Concr. Res. 73 (2015) 228-237.
[36] J. Szczerba, R. Prorok, E. Sniezek, D. Madej, K. Maslona, Influence of time and temperature on ageing and phases synthesis in the $MgO\backslash SiO_2\backslash H_2O$ system, Thermochim. Acta 567 (2013) 57-64.
[37] G.V.P. Bhagath Singh, K.V.L. Subramaniam, Method for direct determination of glassy phase dissolution in hydrating fly ash-cement system using x-ray diffraction, J. Amer. Ceram. Soc. 100(1) (2017) 403-412.

[38] G.V.P. Bhagath Singh, K.V.L. Subramaniam, Quantitative XRD study of amorphous phase in alkali activated low calcium siliceous fly ash, Constr. Build. Mater. 124 (2016) 139-147.
[39] V. Vagvolgyi, R.L. Frost, M. Hales, A. Locke, J. Kristof, E. Horvath, Controlled rate thermal analysis of hydromagnesite, J. Therm. Anal. Calorim. 92 (2008) 893-897.
[40] L.A. Hollingbery, T.R. Hull, The thermal decomposition of huntite and Hydromagnesite-a review, Thermochim. Acta 509 (2010) 1-11.
[41] R.L. Frost, S.J. Palmer, Infrared and infrared emission spectroscopy of nesquehonite Mg(OH) (HCO_3) $2H_2O$-implications for the formula of nesquehonite, Spectrochim. Acta A Mol. Biomol. Spectrosc. 78 (2011) 1255-1260.
[42] G. Jauffret, J. Morrison, F. Glasser, On the thermal decomposition of nesquehonite, J. Therm. Anal. Calorim. 122 (2015) 601-609.
[43] P. Ballirano, C. De Vito, V. Ferrini, S. Mignardi, The thermal behaviour and structural stability of nesquehonite, $MgCO_3 \cdot 3H_2O$, evaluated by in situ laboratory parallel-beam X-ray powder diffraction: new constraints on CO_2 sequestration within minerals, J. Hazard. Mater. 178 (2010) 522-528.
[44] R.L. Frost, S. Bahfenne, J. Graham, W.N. Martens, Thermal stability of artinite, dypingite and brugnatellite-implications for the geosequestration of green house gases, Thermochim. Acta 475 (2008) 39-43.
[45] R. Zhang, D.K. Panesar, Investigation on Mg content in calcite when magnesium calcite and nesquehonite co-precipitate in hardened paste, Thermochimica Acta 654 (2017) 203-215.
[46] H. Ren, Z. Chen, Y. Wu, M. Yang, J. Chen, H. Hu, J. Liu, Thermal characterization and kinetic analysis of nesquehonite, hydromagnesite, and brucite, using TG–DTG and DSC techniques, J. Therm. Anal. Calorim. 115(2) (2014) 1949-1960.
[47] C. Kuenzel, F. Zhang, V. Ferrandiz-Mas, C.R. Cheeseman, E.M. Gartner, The mechanism of hydration of MgO-hydromagnesite blends, Cem. Concr. Res. 103 (2018) 123-129.
[48] R.L. Frost, J.T. Kloprogge, Infrared emission spectroscopic study of brucite, Spectrochim. Acta A Mol. Biomol. Spectrosc. 55 (1999) 2195-2205.
[49] B.P. Choudhari, M.C. Vaidya, D.S. Datar, Physico-chemical studies on basic magnesium carbonates, Indian J. Chem. 10 (1972) 731-733.

785 [50] Y. Sawada, J. Yamaguchi, O. Sakurai, K. Uematsu, N. Mizutani, M. Kato,
786 Thermal decomposition of basic magnesium carbonates under high-pressure gas
787 atmospheres, Thermochim. Acta 32 (1979) 277-291.
788 [51] G. Raade, Dypingite, a new hydrous basic carbonate of magnesium, from
789 Norway, Am. Minerol. 88 (1970) 1457.
790 [52] W.B. White, Infrared characterization of water and hydroxyl ion in the basic
791 magnesium carbonate minerals, Am. Mineral. 56 (1971) 46-53.
792 [53] H.G.M. Edwards, S.E. Jorge Villar, J. Jehlicka, T. Munshi, FT-Raman
793 spectroscopic study of calcium-rich and magnesium-rich carbonate minerals,
794 Spectrochim. Acta A 61 (2005) 2273-2280.
795 [54] B.E. Scheetz, W.B. White, Vibrational spectra of the alkaline earth double
796 carbonates, Am. Mineral. 62 (1977) 39-50.
797 [55] D. Nied, K. Enemark-Rasmussen, E. L'Hopital, J. Skibsted, B. Lothenbach,
798 Properties of magnesium silicate hydrates (MSH) Cem. Concr. Res. 79 (2016),
799 pp. 323-332.
800 [56] E. Bernard, B. Lothenbach, C. Chlique, M. Wyrzykowski, A. Dauzères, I.
801 Pochard, C. Cau-Dit-Coumes, Characterization of magnesium silicate hydrate (M-
802 S-H), Cem. Concr. Res. 116 (2019) 309-330.
803 [57] P. Yu, R.J. Kirkpatrick, B. Poe, P.F. McMillan, X. Cong, Structure of calcium
804 silicate hydrate (C-S-H): near-, mid-, and far-infrared spectroscopy, J. Am. Ceram.
805 Soc. 82 (1999) 742-748.

List of Tables

Table 1 Chemical compositions and physical properties of MgO and MS (i.e. % by mass).

Compounds	MgO	MS
	Composition (%)	
SiO_2	0.49	86.28
Al_2O_3	0	1.95
CaO	1.11	2.94
Fe_2O_3	0.37	0
MgO	91.24	2.09
SO_3	1.17	2.34
P_2O_5	0.98	0.89
Na_2O	4.13	1.67
K_2O	0.39	1.68
Specific surface area (m^2/g)	36.7	16.9
LOI (%)	6.3	2.2

Table 2 Different size fractions of MgO, MS and hydromagnesite seeds.

Material	Size (μm)		
	d_{10}	d_{50}	d_{90}
MgO	1.05	13.65	50.48
MS	17.28	87.61	273.12
Hydromagnesite seed	6.53	17.89	66.28

Table 3 The binder compositions (i.e. % by mass) used in the preparation of samples.

Mix	MgO (%)	MS (%)	Seed (%)
MgO	100	0	0
MgO-HM	99	0	1
MgO-MS	50	50	0
MgO-MS-HM	49.5	49.5	1
OPC	100	0	0

Table 4 Quantification of phases within MgO, MS and hydromagnesite seed.

Material	Periclase (%)	Magnesite (%)	Hydromagnesite (%)	Reactive SiO_2 (%)	Glassy portion (%)
MgO	96.5	3.5	-	-	-
MS	-	-	-	84.3	99.9
Hydromagnesite seed	-	-	100	-	-

Table 5 Peak positions of the glassy portions of MS and synthesized M-S-H.

Material	Peak position-I (º)	Peak position-II (º)	Peak position-III (º)
MS	21.72 ± 0.23	-	-
M-S-H	25.20 ± 0.18	35.77 ± 0.20	60.13 ± 0.17

Table 6 Quantification of phases (%) within MgO samples cured under sealed and carbonated conditions for 3 and 28 days. The standard deviation results were shown in () next to each value.

Composition (%)	Sealed				Carbonated			
	MgO		MgO-HM		MgO		MgO-HM	
	3 days	28 days	3 days	28 days	3 days	28 days	3 days	28 days
Periclase	40.8(1.1)	14.3(1.9)	39.1(1.7)	13.4(2.1)	30.6(1.9)	11.3(1.7)	29.3(2.4)	10.0(1.7)
Magnesite	1.7(0.3)	1.8(0.4)	1.7(0.2)	1.7(0.4)	1.9(0.8)	2.2(0.7)	1.9(0.3)	2.3(0.7)
Brucite	56.7(1.8)	83.5(1.7)	58.0(2.1)	83.4(1.6)	65.7(2.0)	84.1(1.7)	67.1(1.8)	85.2(1.9)
Artinite	0.0	0.0	0.0	0.0	0.7(0.2)	0.8(0.3)	0.9(0.4)	0.9(0.2)
Dypingite	0.0	0.0	0.0	0.0	0.4(0.2)	1.1(0.5)	0.4(0.1)	1.1(0.3)
Hydromagnesite	0.0	0.0	0.6(0.2)	1.0(0.4)	0.5(0.2)	0.3(0.2)	0.5(0.2)	0.4(0.1)
Nesquehonite	0.0	0.0	0.0	0.0	0.1(0.1)	0.2(0.1)	0.2(0.1)	0.3(0.1)

Table 7 Quantification of phases (%) within MgO-MS samples cured under sealed and carbonated conditions for 3 and 28 days. The standard deviation results were shown in () next to each value.

Composition (%)	Sealed				Carbonated			
	MgO-MS		MgO-MS-HM		MgO-MS		MgO-MS-HM	
	3 days	28 days	3 days	28 days	3 days	28 days	3 days	28 days
Periclase	16.7(1.4)	7.8(1.2)	16.2(0.9)	6.8(0.8)	16.0(1.4)	5.9(0.4)	15.9(1.8)	6.4(1.2)
Magnesite	0.8(0.2)	1.6(0.9)	1.5(0.5)	1.7(0.4)	0.7(0.4)	1.5(0.7)	1.1(0.6)	1.3(0.7)
Brucite	0.9(0.1)	2.9(0.7)	1.3(0.4)	1.5(0.7)	0.8(0.2)	2.7(0.8)	1.7(0.4)	2.5(1.1)
Hydromagnesite	0.0	0.0	0.2(0.1)	0.4(0.1)	0.7(0.2)	0.9(0.3)	1.4(0.7)	1.8(0.5)
Dypingite	0.0	0.0	0.0	0.0	0.0	0.2(0.1)	0.5(0.1)	0.8(0.2)
Nesquehonite	0.0	0.0	0.0	0.0	0.0	1.0(0.7)	0.0	0.0
Unreacted silica	37.0(1.8)	24.5(2.3)	36.0(1.9)	19.5(2.2)	36.8(1.7)	21.8(2.5)	32.3(1.9)	14.1(2.1)
M-S-H	44.5(1.8)	63.0(2.3)	44.8(1.9)	70.0(2.2)	45.0(1.7)	66.7(2.5)	46.8(1.9)	73.9(2.1)

Table 8 Mass loss values observed in all samples by using TGA.

Curing condition	Mix	Mass loss (%)							
		50-340 °C		340-480 °C		480-600 °C		600-700 °C	
		3 days	28 days	3 days	28 days	3 days	28 days	3 days	28 days
Sealed	MgO	1.7	2.0	17.1	25.3	1.0	1.2	1.0	1.1
	MgO-HM	2.3	2.5	18.1	25.6	1.3	1.4	1.4	1.6
	MgO-MS	9.8	11.8	3.5	4.2	2.1	2.7	0.5	0.8
	MgO-MS-HM	9.5	11.2	3.6	4.3	2.5	2.6	0.6	0.9
Carbonated	MgO	1.6	2.4	21.6	26.9	2.3	2.8	1.4	1.5
	MgO-HM	2.5	2.7	21.9	27.1	2.0	2.1	1.5	2.0
	MgO-MS	10.9	12.5	3.3	4.2	2.0	2.5	1.4	1.7
	MgO-MS-HM	10.7	12.4	3.4	4.3	2.0	2.5	1.3	1.9

Table 9 Comparison of brucite contents obtained via TGA and XRD-Rietveld refinement.

Curing condition	Mix	Brucite content (%)			
		TGA		Rietveld analysis	
		3 days	28 days	3 days	28 days
Sealed	MgO	55.4	82.0	56.7	83.5
	MgO-HM	58.7	82.9	58	83.4
	MgO-MS	11.3	13.6	0.9	2.9
	MgO-MS-HM	11.7	13.9	1.3	1.5
Carbonated	MgO	69.9	87.1	65.7	84.1
	MgO-HM	70.9	87.6	67.1	85.2
	MgO-MS	10.7	13.6	0.8	2.7
	MgO-MS-HM	11.0	13.9	1.7	2.5

Table 10 Band locations of MS, synthesized M-S-H and hydrated MgO-MS sample.

Sample	Wavelength (cm^{-1})
MS	1040±20, 1105±20, 1180±10
Synthesized M-S-H	890±10, 980±15, 1015±15
MgO-MS sample	900±10, 990±10, 1060±15, 1120±10, 1160±15

List of Figures

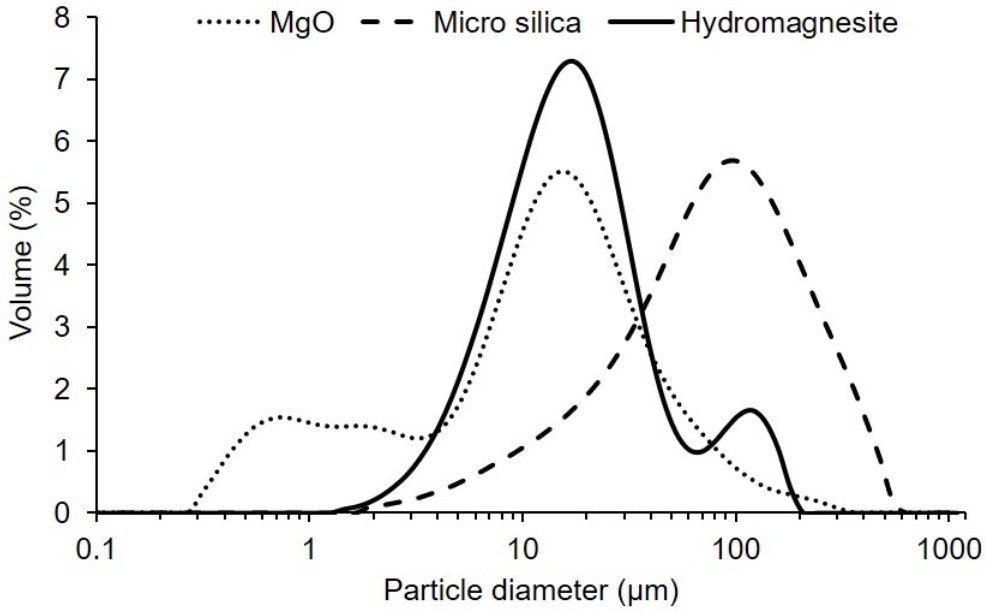

Fig. 1. Particle size distributions of MgO, MS and hydromagnesite seed.

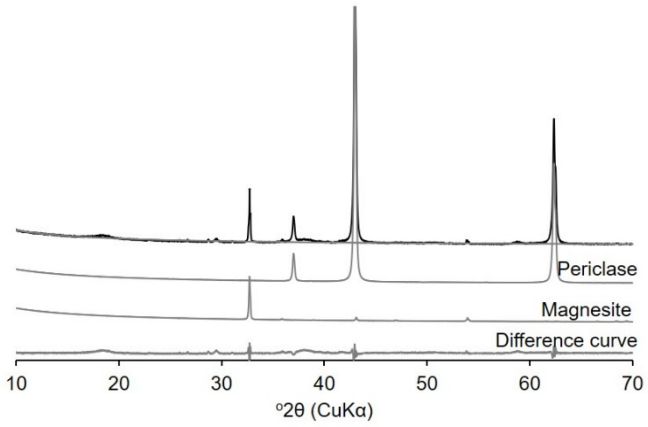

(a)

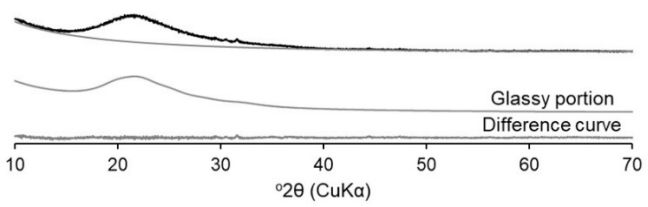

(b)

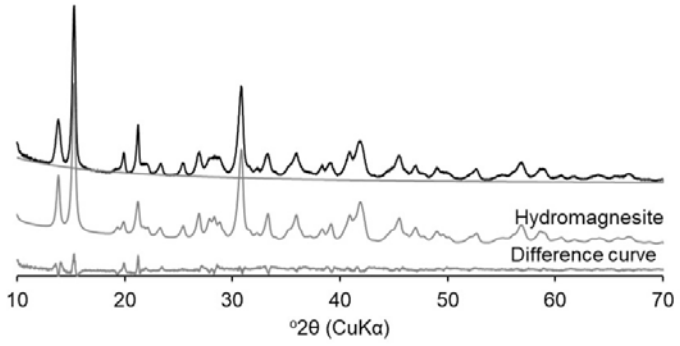

(c)

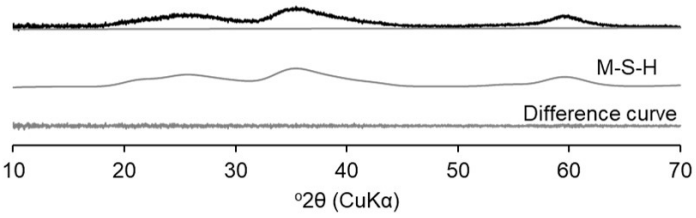

(d)

Fig. 2. XRD patterns* of (a) MgO, (b) MS, (c) hydromagnesite seed and (d) synthesized M-S-H.

* The refined phases are also shown in each figure.

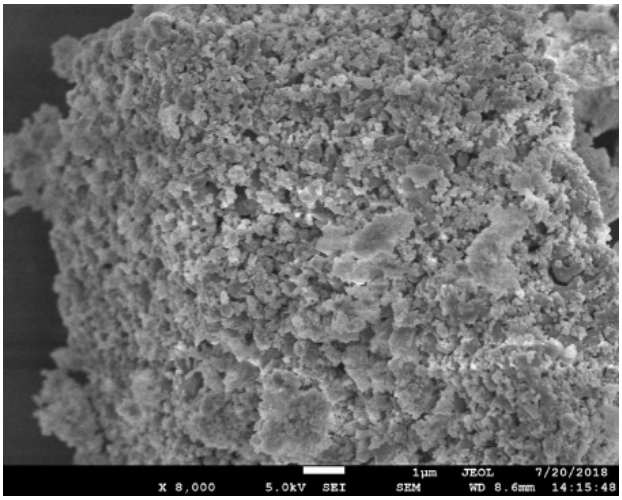

(a)

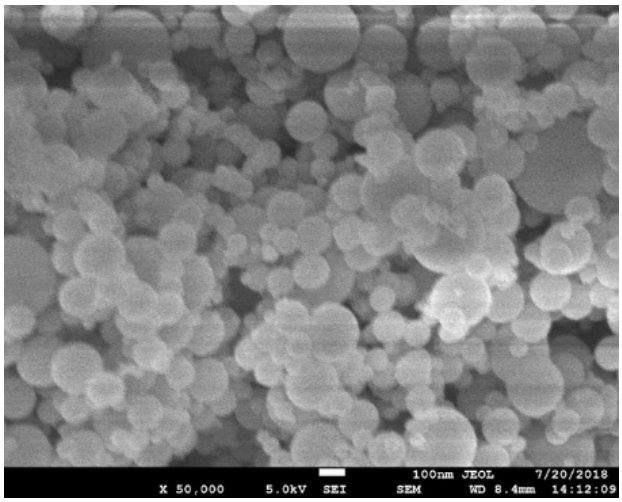

(b)

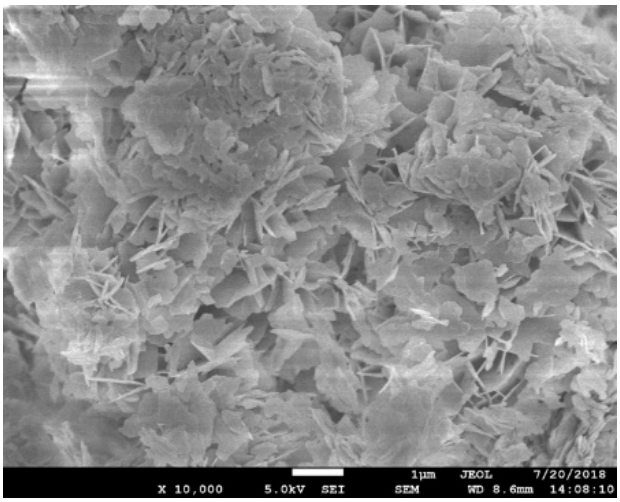

(c)

Fig. 3. SEM images of (a) MgO, (b) MS and (c) hydromagnesite seed.

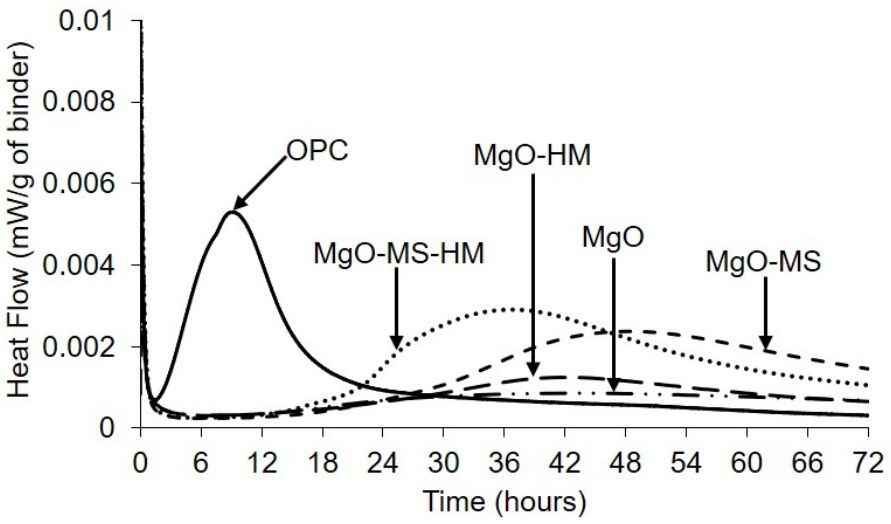

(a)

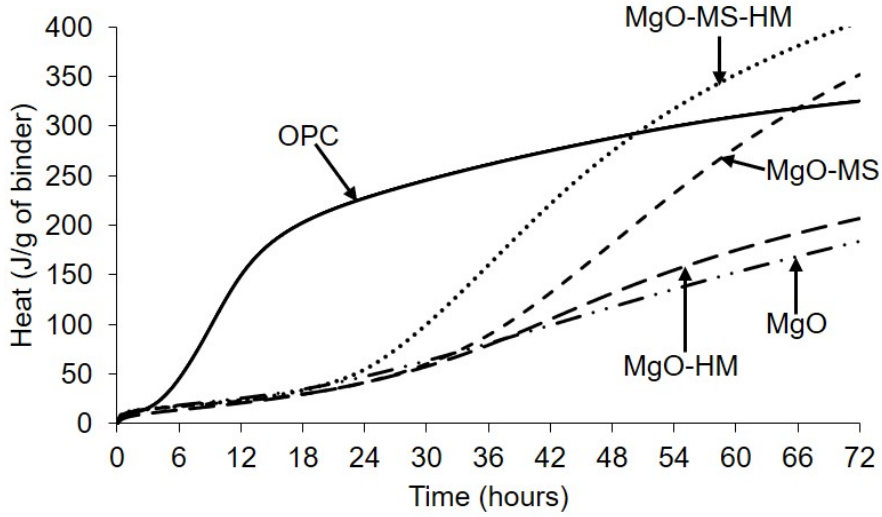

(b)

Fig. 4. Isothermal calorimetry results showing the (a) heat flow and (b) cumulative heat of paste samples.

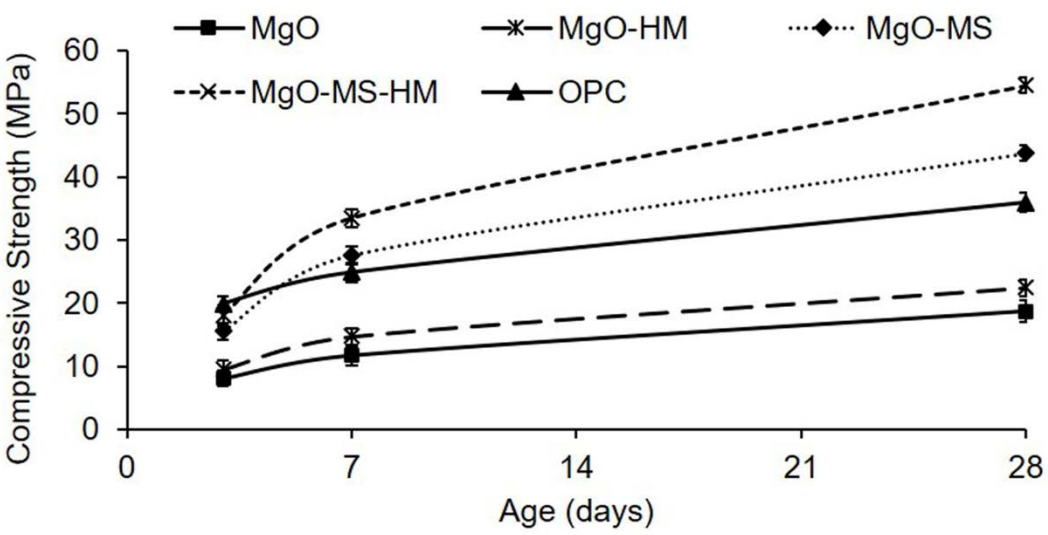

(a)

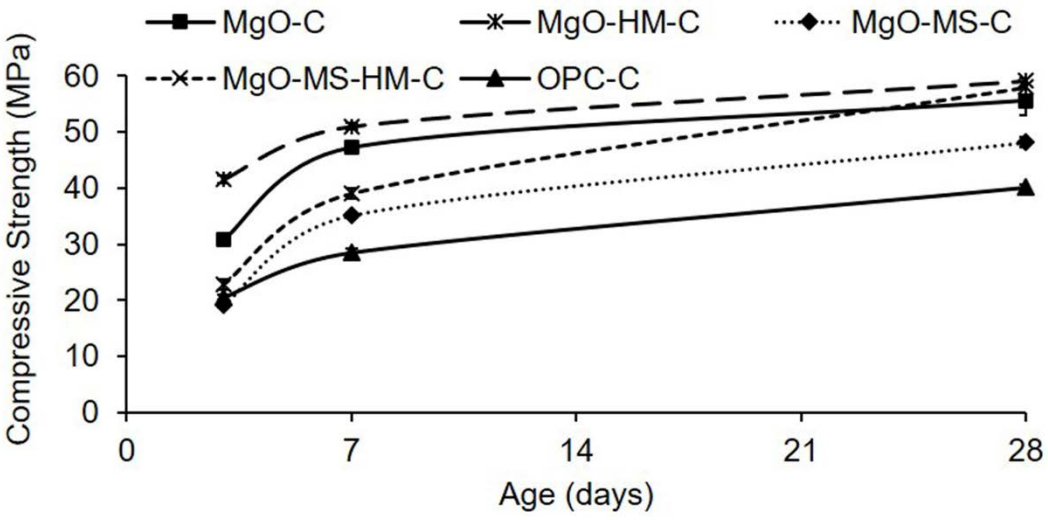

(b)

Fig. 5. Compressive strengths of concrete mixes, showing the effect of seeding under (a) sealed and (b) carbonation curing.

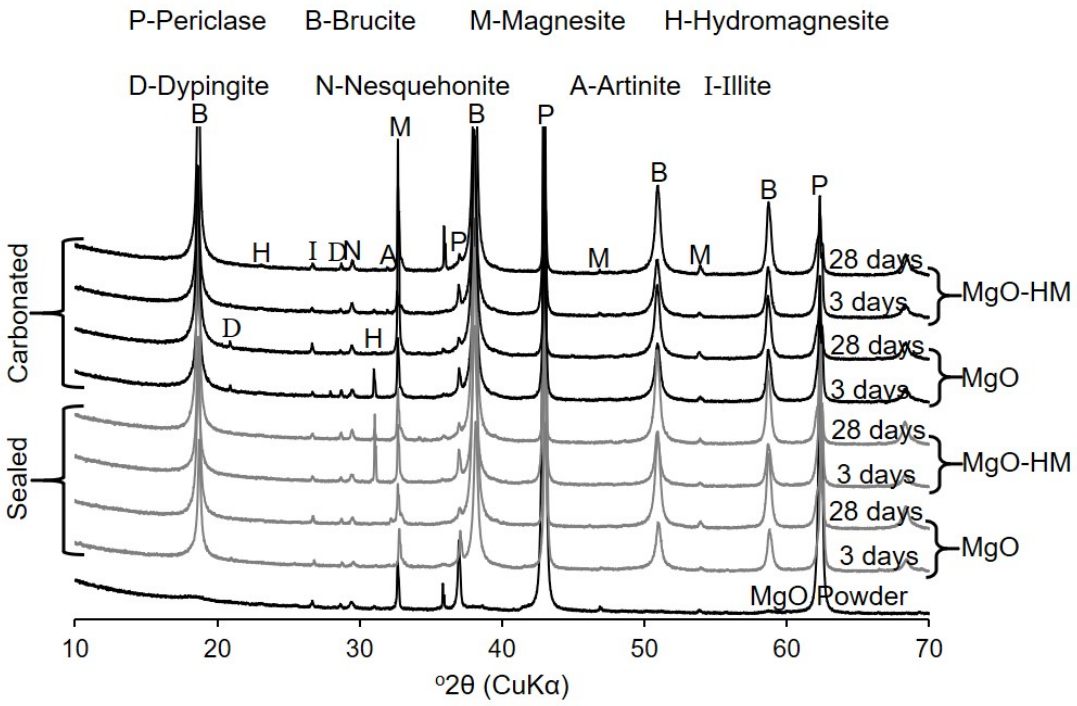

(a)

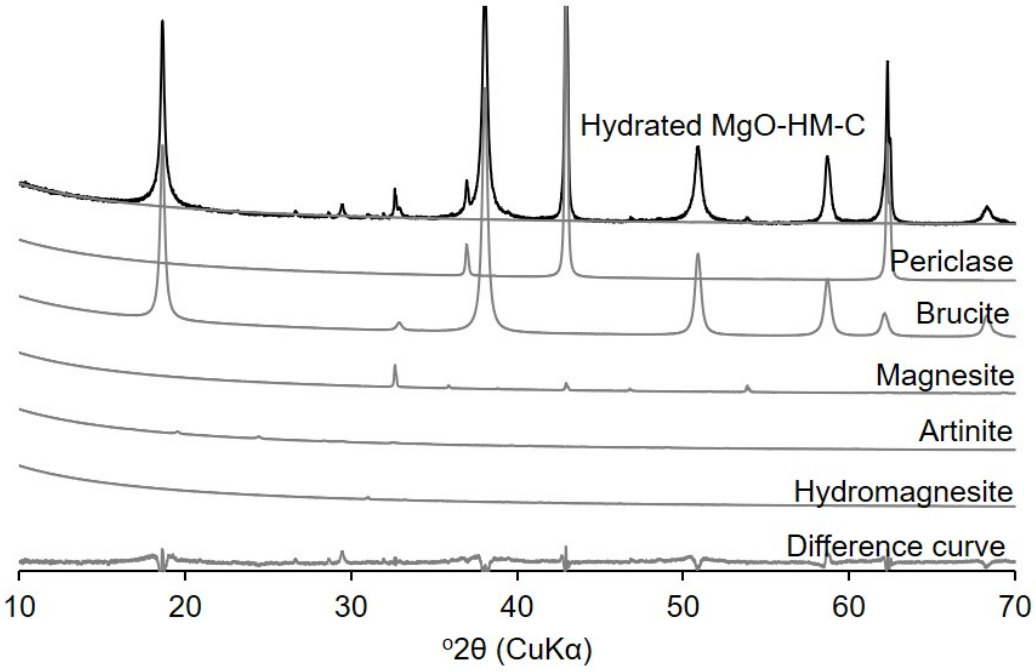

(b)

Fig. 6. XRD patterns of (a) all MgO samples cured under sealed and carbonated conditions for 3 and 28 days and (b) the refined spectra of MgO-HM sample cured under carbonated conditions for 3 days, including the individual refined phases.

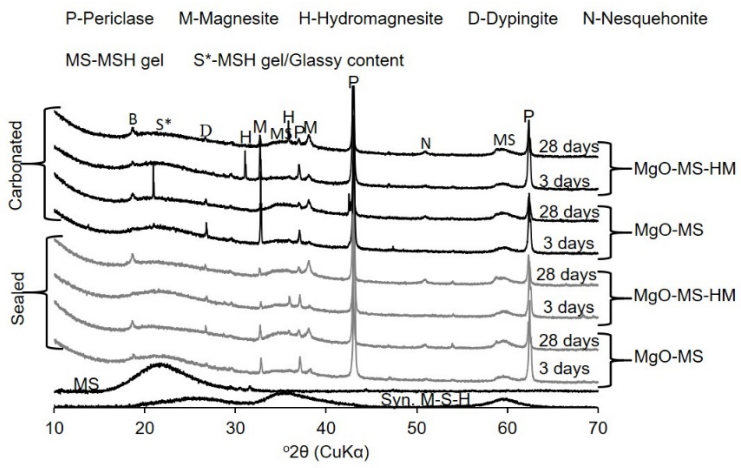

(a)

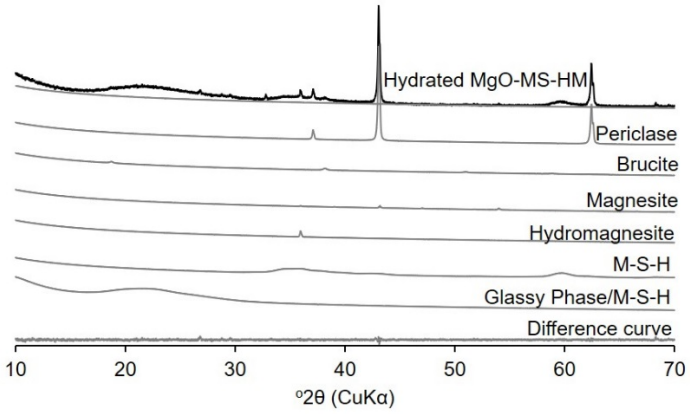

(b)

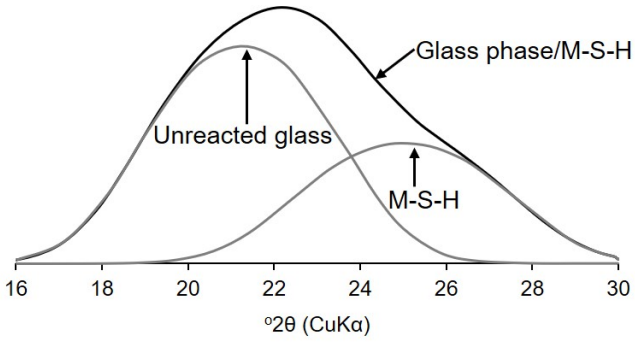

(c)

Fig. 7. XRD patterns of (a) all MgO-MS samples cured under sealed and carbonated conditions for 3 and 28 days, (b) the refined spectra of MgO-MS-HM sample cured under sealed conditions for 3 days, including the individual refined phases and (c) deconvolution of unreacted glass and M-S-H

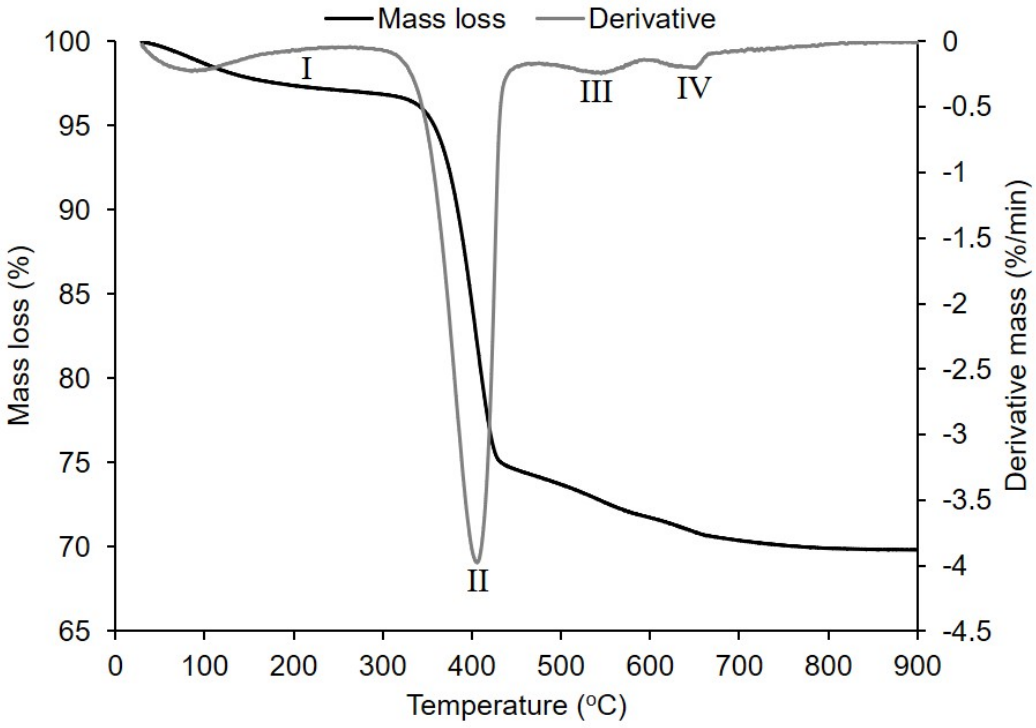

(a)

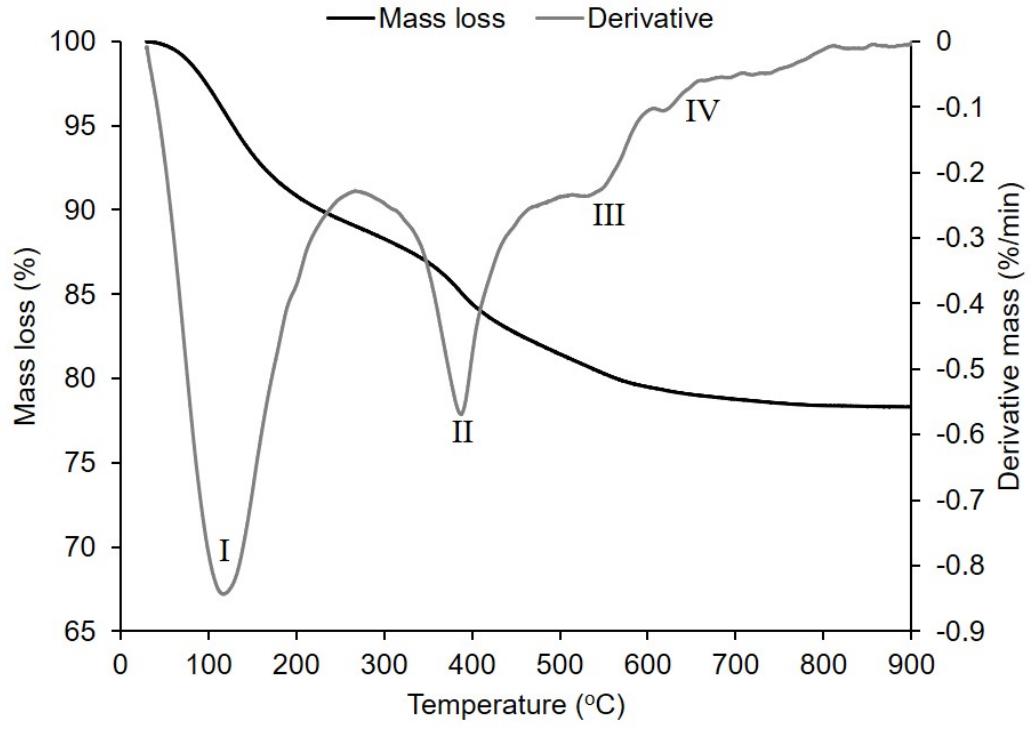

(b)

Fig. 8. Typical TG/DTG curves of (a) MgO and (b) MgO-MS samples cured under carbonated conditions for 28 days.

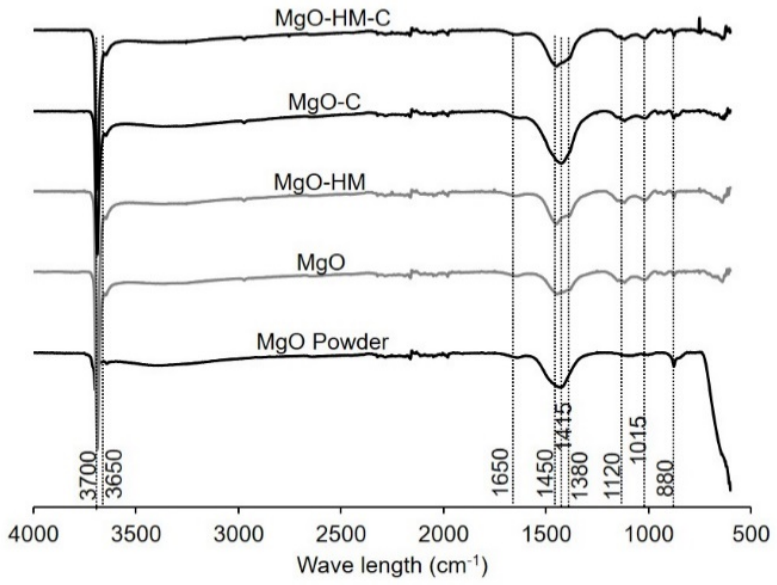

(a)

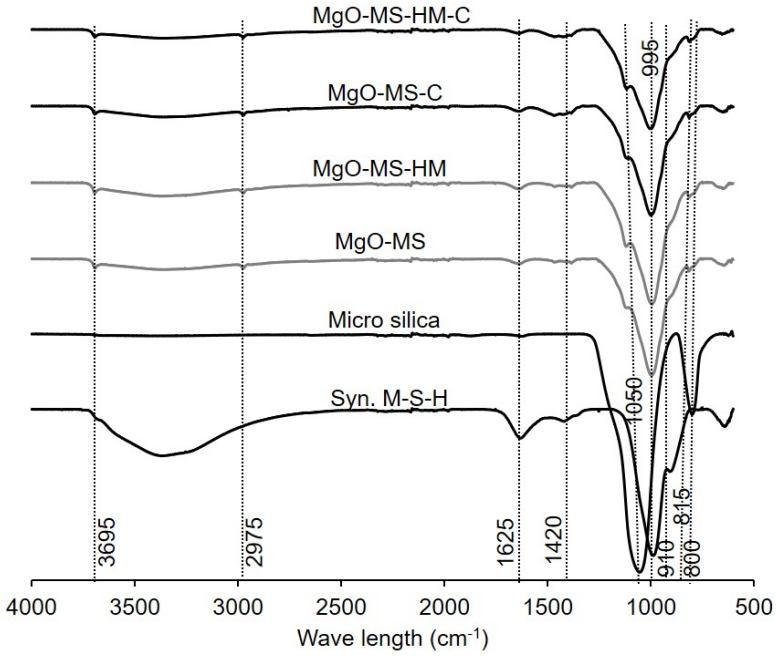

(b)

Fig. 9. FTIR spectra of (a) MgO and (b) MgO-MS samples with and without the addition of seeds, cured under sealed and carbonated conditions for 28 days.

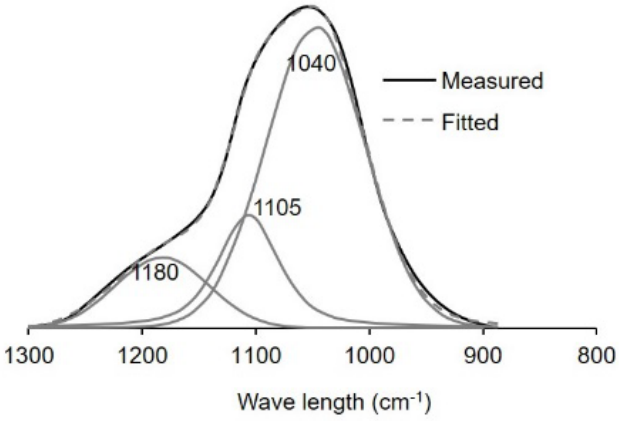

(a)

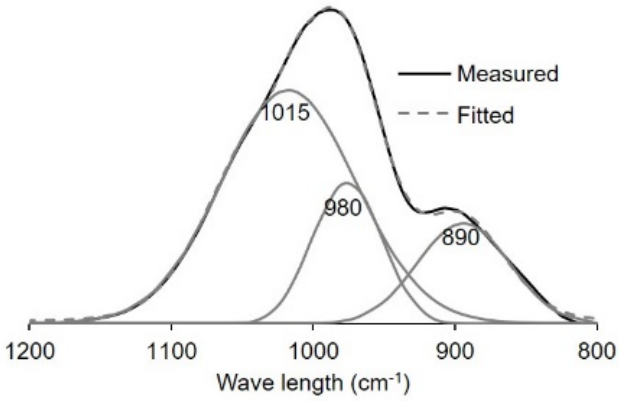

(b)

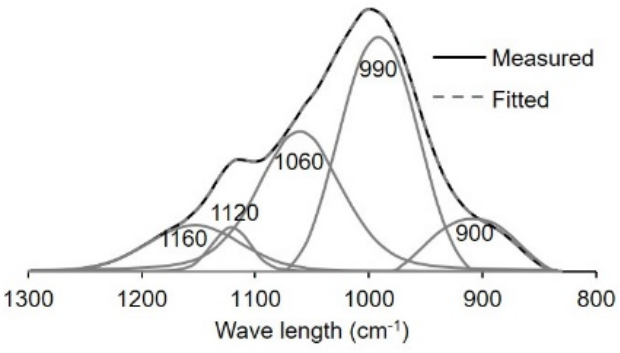

(c)

Fig. 10. Deconvoluted band positions of (a) MS, (b) synthesized M-S-H and (c) MgO-MS sample cured under sealed conditions for 28 days.

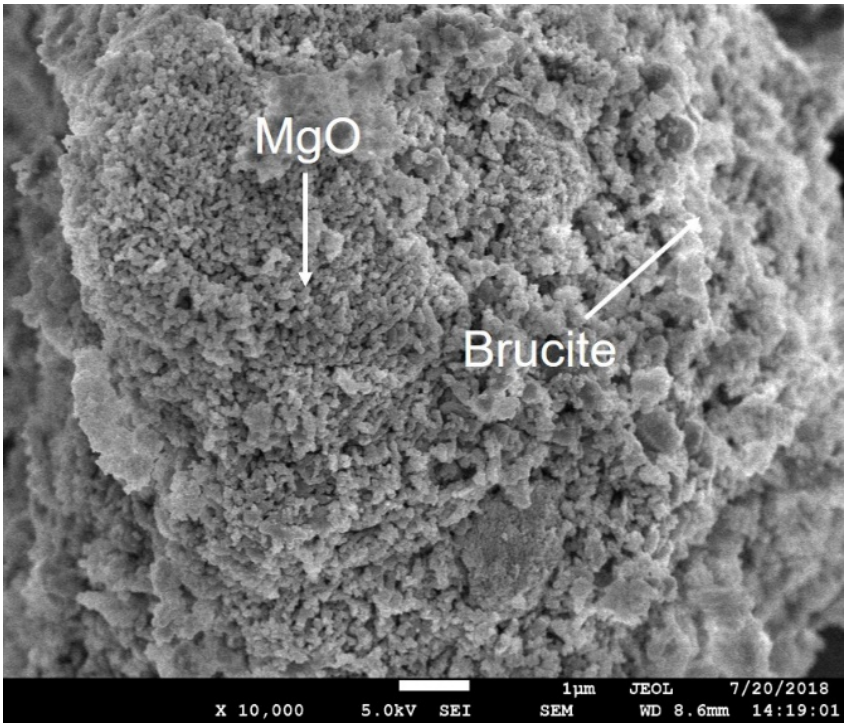

(a)

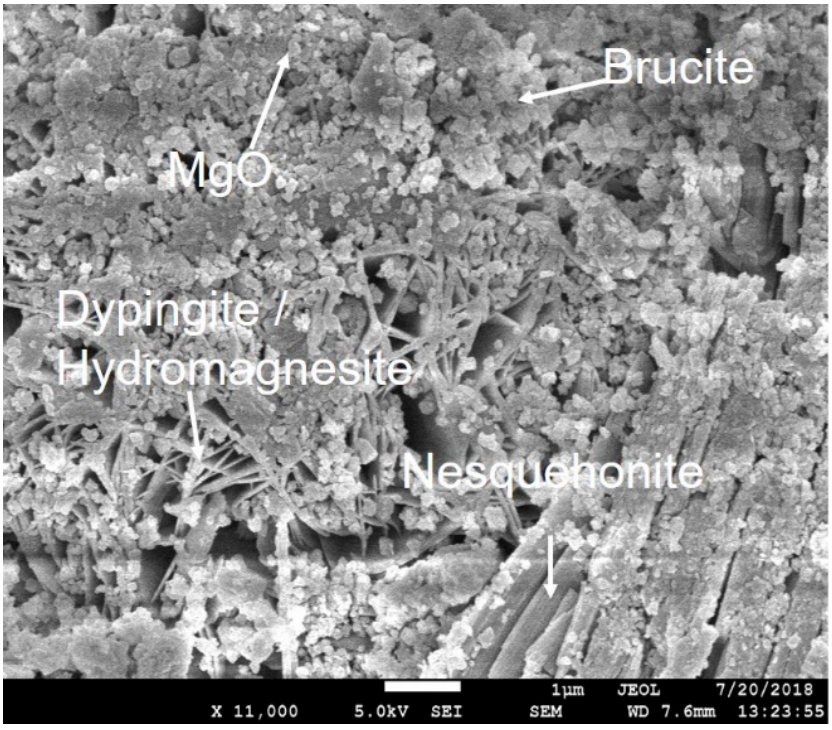

(b)

Fig. 11. SEM images of MgO samples cured under (a) sealed and (b) carbonated conditions for 28 days.

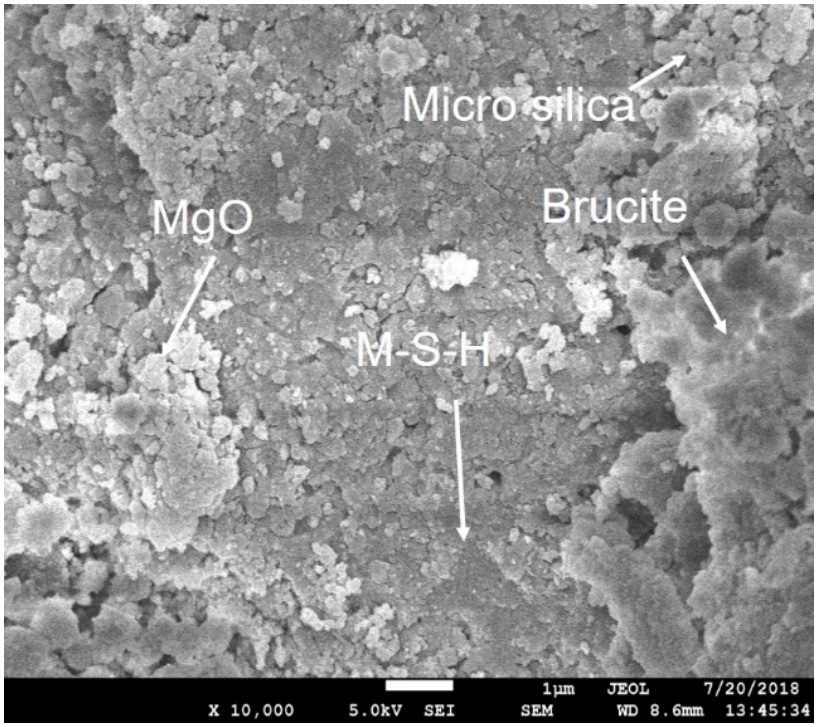

(a)

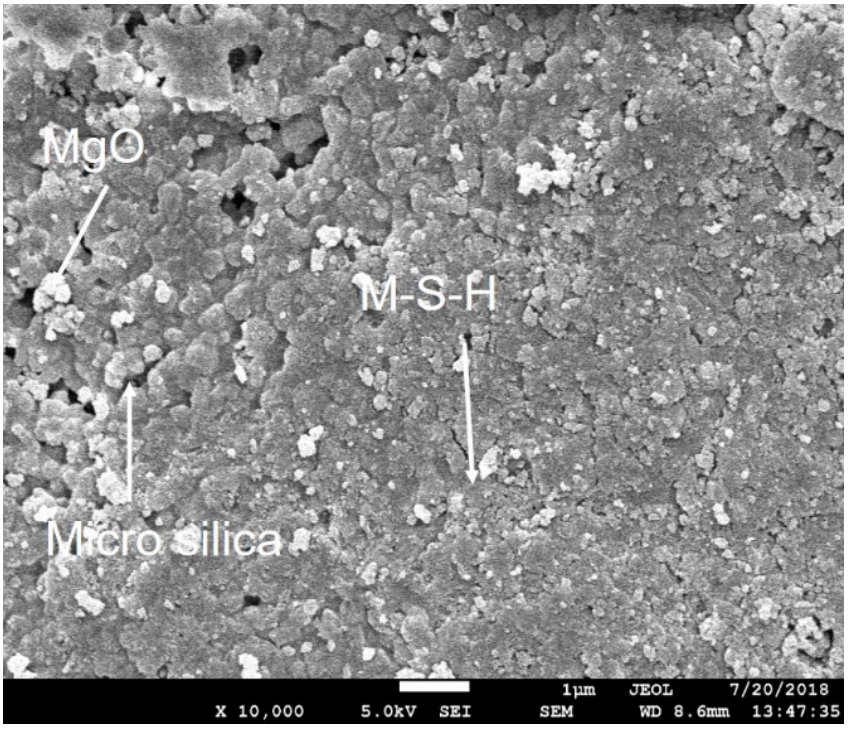

(b)

Fig. 12. SEM images of (a) MgO-MS and (b) MgO-MS-HM samples cured under sealed conditions for 28 days.